Modeling and Design of RFID-Controlled Binary-Reconfigurable Frequency Selective Surfaces

Francesco Lestini, *Member, IEEE*, Gaetano Marrocco, *Senior Member, IEEE*, and Cecilia Occhiuzzi, *Member, IEEE*

***Abstract*—Radiofrequency Identification (RFID) technology is entering its third generation, extending beyond identification and sensing toward the *control* of electromagnetic (EM) functions. Recent studies have demonstrated the feasibility of RFID-controlled antennas, metasurfaces, and intelligent surfaces, where standard RFID Integrated Circuits (ICs) act as wireless, battery-free controllers. Within this family, *Frequency Selective Surfaces* (FSSs) represent a particularly demanding case, since their narrowband resonant response must be precisely engineered under the discrete bias conditions imposed by RFID hardware. This paper presents a modeling and synthesis framework for binary-reconfigurable FSSs driven by RFID ICs. By exploiting the two programmable output voltages of commercial chips, the proposed FSS toggles between reflective and transparent states at a fixed frequency, enabling wirelessly programmable interfaces without any external supply. A semi-analytical Equivalent Circuit Model (ECM) links the target specifications—operating frequency and fractional bandwidth—to the lumped circuit parameters and, in turn, to the unit-cell geometry. The model provides a rapid and physically interpretable design tool, validated through full-wave simulations of multiple layouts showing agreement within 5% of numerical results.**

***Index Terms*—Frequency selective surfaces, RFID controller, equivalent circuit model, electromagnetic shielding, reconfigurable FSS.**

I. Introduction

RADIOFREQUENCY Identification (RFID) technology is entering its third generation. After powering a revolution in *identification* and enabling a new class of *sensing* devices, RFID systems are now evolving into platforms for *controlling* the electromagnetic (EM) environment itself—driving reconfigurable, battery-free components and intelligent surfaces. By leveraging the capability of commercial RFID Integrated Circuits (ICs) to harvest energy from the reader's field and to generate programmable DC voltages, passive components such as PIN diodes, varactors, and switches can be wirelessly reconfigured without batteries or wired bias networks [1].

Received 14 October 2025; revised 4 December 2025; accepted 8 December 2025. Date of publication 12 December 2025; date of current version 22 December 2025. This work was supported in part by European Union–NextGenerationEU (Spoke: 2. Flagship Project 7) through the Project Innovation Ecosystem (ECS) 0000024 (Rome Technopole, National Recovery and Resilience Plan (NRRP) Mission 4 Component 2 Investment 1.5) under Grant CUP B83C22002820006 and in part by the Project "SEcurity and RIghts In the CyberSpace—SERICS, Spoke 9" (PE00000014) through the National Recovery and Resilience Plan (NRRP) funded by the European Union–NextGenerationEU under Grant CUP B53C22003990006. *(Corresponding author: Francesco Lestini.)*

The authors are with DICII, University of Rome Tor Vergata, 00133 Rome, Italy (e-mail: francesco.lestini@uniroma2.it).

Digital Object Identifier 10.1109/JRFID.2025.3643593

Within the family of standard RFID ICs, a few devices natively support programmable output voltages. Representative examples include the EM Microelectronic EM4152 [2] and EM4325 [3] families, which provide ultra-low-power DC outputs (up to 1.8–3.3 V in battery-assisted operation) with current levels on the order of a few microamperes. When the harvested RF power exceeds the *operation* threshold (typically between −17 and −15 dBm [4]), the chip delivers a stable bias voltage at its output port that can directly tune reactive components without additional circuitry. Recent studies have also shown that RFID ICs can respond to external interrogation signals not specifically addressed to them, further extending the range of possible powering sources [5].

Early demonstrations for RFID-controlled devices include reconfigurable intelligent surfaces, antennas, beam forming networks and cooperative primary–secondary tag networks, in which commercial RFID ICs are repurposed as passive, uniquely addressable controllers [4], [6], [7], [8], [9], [10], [11]. Among RFID-driven reconfigurable devices, *Frequency Selective Surfaces* (FSSs) represent a particularly effective platform. RFID-enabled FSSs have been demonstrated as suitable solutions for cyber-physical security [12] and wireless power transfer [13], owing to their passive operation, mechanical robustness, and capability to be seamlessly embedded within materials and objects, where wired control is impractical.

FSSs are two-dimensional periodic arrays of metallic or dielectric elements designed to filter EM waves within specific frequency bands [14]. Traditionally employed in radar radomes, reflectors, absorbers, and lenses [15], [16], [17], [18], [19], [20], [21], [22], FSSs have recently been explored as reconfigurable structures for adaptive reflection, electromagnetic shielding, and secure communication [23], [24]. In these contexts, the surface operates as a *binary EM switch* that alternates between a reflective and a transparent state at a fixed frequency f_0, selectively controlling the propagation of incident waves (Fig. 1). Conventional reconfigurable FSSs rely on active components, such as PIN diodes or varactors, biased through wired DC networks, FPGAs, or microcontrollers [25], [26], [27]. Although these architectures provide precise control, their dependence on external power, multiple interconnections, and complex routing strongly limit scalability and long-term autonomy. In contrast, RFID-based driving offers a fully passive alternative: the controller is wirelessly powered through its Over-The-Air (OTA) interface, typically by the

2469-7281 © 2025 IEEE. All rights reserved, including rights for text and data mining, and training of artificial intelligence and similar technologies. Personal use is permitted, but republication/redistribution requires IEEE permission. See https://www.ieee.org/publications/rights/index.html for more information.

Authorized licensed use limited to: Universita degli Studi di Roma Tor Vergata. Downloaded on May 21,2026 at 10:39:51 UTC from IEEE Xplore. Restrictions apply.

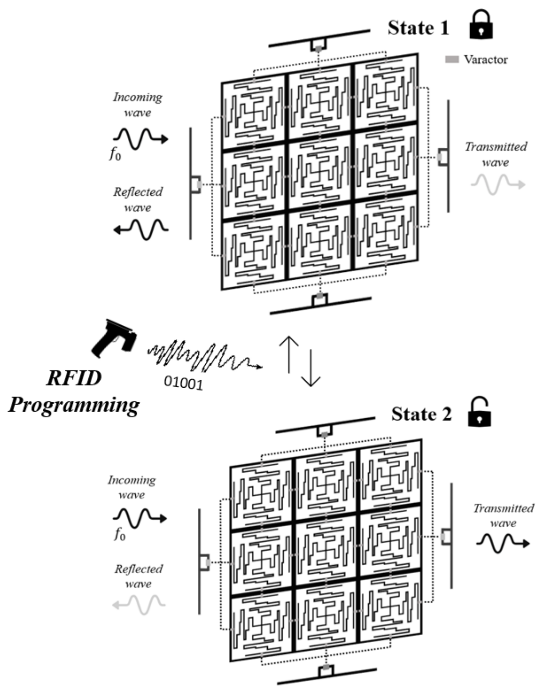

Fig. 1. Conceptual illustration of an RFID-controlled reconfigurable FSS acting as a binary electromagnetic switch. In State 1, the surface reflects the incoming wave at frequency f_0. In State 2, it becomes transparent at the same frequency. Switching between states is driven by the output voltages generated by RFID ICs, which are programmed by an external RFID reader. The ICs can be integrated directly into the FSS layout or connected to a standard UHF tag placed in close proximity to the structure, as shown in this example.

same RF field that illuminates the FSS. However, owing to the stringent constraints of this technology, i.e., the sub-milliwatt power available from passive RFID ICs and the footprint and cost limitations imposed by densely packed FSS unit cells, RFID-driven reconfigurable FSSs must rely only on varactor diodes, which are the only switching elements compatible with both requirements [4].

The FSS state is determined by the discrete control voltages generated at the RFID IC output ports [1]. Since commercial chips provide only two programmable voltage levels, the attainable tuning is inherently *binary*, corresponding to two distinct capacitance states of the varactor. This constraint enables switching between reflection and transmission at a fixed frequency f_0, but it also imposes a fundamental shift in the design paradigm: unlike conventional biasing schemes, where the control voltage can be continuously adjusted to reach the desired response, RFID-based tuning is intrinsically *blind*—the two states must be pre-engineered so that the target electromagnetic behavior emerges *a priori* from fabrication.

To overcome these limitations, this work introduces an analytical synthesis framework based on an *Equivalent Circuit Model* (ECM) that directly links the discrete capacitance states imposed by the RFID controller to the electromagnetic response of the surface. The proposed methodology enables rapid prediction of reflection and transmission characteristics of binary FSSs from high-level specifications—target frequency f_0 and desired fractional bandwidth (FBW)—and their direct translation into geometric parameters, avoiding time-consuming full-wave iterations.

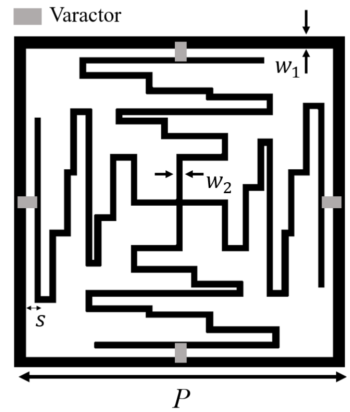

Fig. 2. Generalized unit-cell layout with an inductive outer loop and an arbitrary inner resonator, connected via varactor diodes for binary reconfigurability.

The remainder of this paper is organized as follows. Section II introduces the RFID-driven FSS architecture and its ECM formulation. Section III validates the model through full-wave analysis of three representative geometries—concentric loops, Jerusalem cross, and folded cross—demonstrating its capability to predict the binary response with high accuracy. The Appendix provides additional analytical insights into the achievable periodicity, bandwidth, and selection of suitable varactors for RFID-controlled reconfigurability.

II. FSS Layout and Equivalent Circuit Model

The proposed model applies to FSSs whose unit cells comprise a subwavelength element enclosed by an external inductive loop (Fig. 2). The inner layout may adopt a variety of geometries composed of conductive traces oriented parallel and orthogonal to the surrounding frame. To ensure stable electromagnetic performance regardless of the wave polarization and angle of incidence (an essential requirement in practical implementations), a circular geometrical symmetry is assumed for the internal path. Traces are connected to the frames through varactors, circularly symmetric as well, and in turn controlled by RFID IC (included in Fig. 2 in the external tag placed close to the cell). These layouts are particularly suited for reconfigurable implementations, as the varactors can be placed between the central layout and the outer loop to allow parallel biasing, thus simplifying the DC routing and requiring only a single RF choke for RF/DC isolation [26]. Moreover, this configuration also enables distinct frequency-selective responses based on the varactor's tuning state, with discrete capacitance values allowing reliable switching between bandstop and bandpass behaviors. The model will hence derive conditions among the ECM lumped parameters to achieve the desired two-state behaviour at a specified frequency f_0 within the desired FBW in the transparent state.

By considering a set of simplifying assumptions, the unit cell geometry shown in Fig. 2 can be described by the lumped-element circuit model in Fig. 3. First, the analysis considers a linearly polarized Transverse Electromagnetic (TEM) plane wave normally impinging on the FSS, which is assumed to operate in free space. Moreover, varactor diodes are considered as variable capacitors, switching between two different states

Authorized licensed use limited to: Universita degli Studi di Roma Tor Vergata. Downloaded on May 21,2026 at 10:39:51 UTC from IEEE Xplore. Restrictions apply.

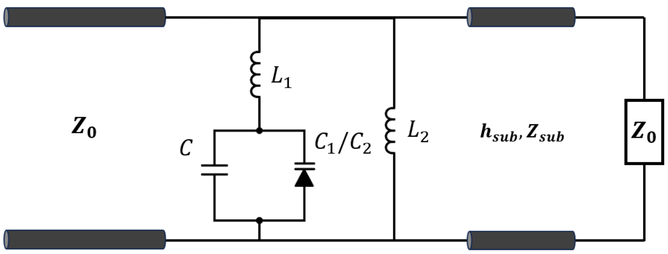

Fig. 3. Equivalent circuit model of the binary reconfigurable FSS. The dielectric substrate is modeled through a transmission line with length h_{sub} and characteristic impedance Z_{sub}.

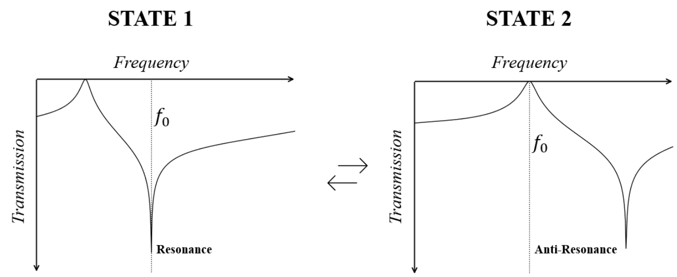

Fig. 4. Transmission behavior of the reconfigurable FSS in the two programmable states. At f_0, the structure exhibits a resonance in State 1 (reflection) and an anti-resonance in State 2 (transmission).

$\{C_1, C_2\}$, which is a standard assumption in equivalent circuit formulations [26], [28], [29], [30]. Finally, the periodicity P of the unit cell is assumed to satisfy the sub-λ approximation, i.e., it must smaller than the operational wavelength ($P < \lambda$), and significantly larger than the width of the conductive traces ($P \gg w_1, w_2$), to guarantee the validity and reliability of the ECM. It is worth noting that the model remains predictive up to $P/\lambda \approx 0.2-0.3$, as confirmed in Section III.

In this model, the internal inductive layout in Fig. 2 is represented by the L_1C series branch, while the loop surrounding it is captured by an additional inductance L_2 placed in parallel. Specifically, L_1 corresponds to the equivalent inductance of the internal arms, and C accounts for the capacitance formed between those arms and the nearby loop. Varactor diodes (C_1, C_2) are considered in parallel with C since the physical gap between the two conductive structures can be regarded as a two-node interface where two displacement-current paths coexist: (i) the *geometrical capacitance* C due to the facing metallic edges, and (ii) the *varactor junction capacitance* $C_i(V)$ bridging the same nodes. Since both elements are connected across the same potential difference, they form parallel branches in the equivalent circuit.

Free space is modeled through a transmission line with characteristic impedance $Z_0 = 377\,\Omega$, while the dielectric substrate on which the FSS is printed, is here modeled through a transmission line with length h_{sub} and characteristic impedances $Z_{sub} = Z_0/\sqrt{\varepsilon_r}$, where ε_r is the relative permittivity of the dielectric.

It is worth noticing that the proposed ECM intentionally adopts a simplified and compact form to enable rapid synthesis and analytical insight. Effects such as manufacturing tolerances, varactor spread, dielectric losses ($\tan\delta$), and temperature variations are therefore not explicitly included in the analytical formulation but can be interpreted as small perturbations of the lumped parameters L_1, L_2, and $C_\parallel$.

A. Formulation

The LC-resonant circuit shown in Fig. 3 is described by an equivalent input impedance Z_{eq} given by:

$$Z_{\mathrm{eq,i}} = \frac{j\omega L_2\left(1-\omega^2 C_{\parallel,i} L_1\right)}{1-\omega^2\left(L_2 C_{\parallel,i} + jL_1 C_{\parallel,i}\right)}, \tag{1}$$

where $C_{\parallel,i} = C + C_i$ ($i = 1, 2$) is the effective capacitance in the i-th programmable state. The structure behaves as a second-order bandpass filter, whose frequency response is characterized by two critical points that depend on the varactor state:

- A *resonant frequency* f_r, at which the input impedance vanishes (short-circuit), producing a strong reflection:

$$f_{r,i} = \frac{1}{2\pi\sqrt{L_1 C_{\parallel,i}}}; \tag{2}$$

- An *anti-resonant frequency* f_{ar}, at which the input admittance is null (open-circuit, namely no interaction), corresponding to a highly transmissive state:

$$f_{ar,i} = \frac{1}{2\pi\sqrt{(L_1+L_2)C_{\parallel,i}}}. \tag{3}$$

To achieve the dual-mode behaviour of the FSS, the equivalent electric parameters of the periodic cell must be selected so that the resonance frequency of State 1 (reflection) and the anti-resonance frequency of State 2 (transmission) are coincident with the working frequency f_0 (Fig. 4). Accordingly, the condition is achieved by enforcing:

$$f_0 = f_{r,1} = f_{ar,2} \tag{4}$$

In addition to the operational frequency f_0, the desired FBW, which characterizes the filter's spectral selectivity around its center frequency, can be imposed as well. Due to the proposed circuit topology (second-order bandpass), the filter's center frequency is naturally identified as the frequency at which the admittance vanishes, i.e., the anti-resonance [31], [32]. Moreover, since the desired switching behavior specifically imposes the anti-resonance condition at the operating frequency f_0 in State 2, the FBW must therefore be evaluated at $f_{ar,2}$. To compute the FBW, the ECM can be approximated by a simplified LC tank circuit [31]. This simplified model is determined by ensuring the equality of the susceptance slopes of the original circuit and the simplified LC scheme at the center frequency $f_{ar,2}$. Thus, the FBW in the transparent state is expressed as:

$$\mathrm{FBW} = \frac{1}{Q} = \frac{1}{\pi f_{ar,2} C_{eq,2} Z_0}, \tag{5}$$

where $C_{eq,2}$ is given by [26] and [31]:

$$C_{eq,2} = (C + C_2)\left(\frac{L_1+L_2}{L_2}\right)^2. \tag{6}$$

Thus, knowing the filter specification (f_0, FBW) and after selecting the varactor (C_1, C_2), combination of equations (4) and (5) provides a unique, fully determined solution for the

Authorized licensed use limited to: Universita degli Studi di Roma Tor Vergata. Downloaded on May 21,2026 at 10:39:51 UTC from IEEE Xplore. Restrictions apply.

lumped circuit parameters L_1, L_2, C, enabling the straightforward synthesis of the binary reconfigurable FSS.

B. Derivation of the ECM Lumped Elements

From (2) and (3) L_1 and C can be expressed as:

$$L_1 = \frac{1}{\omega_0^2(C + C_1)}\,, \tag{7}$$

$$C = \frac{1}{\omega_0^2(L_1 + L_2)} - C_2\,. \tag{8}$$

Thus, by inserting (8) in (7):

$$L_1 = \frac{1}{\omega_0^2\left(\frac{1}{\omega_0^2(L_1+L_2)} - C_2 + C_1\right)}\,. \tag{9}$$

After some algebraic manipulation, eq. (9) can be written in the form of a second-order equation in the unknown L_1:

$$\omega_0^4 \Delta C L_1^2 + \omega_0^4 \Delta C L_2 L_1 - \omega_0^2 L_2 = 0\,, \tag{10}$$

where $\Delta C = C_1 - C_2$. For admitting a real solution, the following condition on the discriminant must be respected:

$$\Delta = \omega_0^6 L_2 \Delta C \cdot (4 + \omega_0^2 L_2 \Delta C) > 0\,. \tag{11}$$

This condition is always satisfied if $\Delta C > 0$.[1] Thus, the FSS must be in the reflecting state for the higher value of the varactor's capacitance, i.e., when the varactor is not biased or, more generally, when it is biased at the lower voltage.

The solution of equation (10) reads:

$$L_1 = \frac{-\omega_0 L_2 \Delta C + \sqrt{L_2 \Delta C \cdot (4 + \omega_0^2 L_2 \Delta C)}}{2\omega_0 \Delta C}\,, \tag{13}$$

while the capacitance C can be expressed as in (8). Moreover, the inductance L_2 can be related to the FBW from (5) as follows:

$$\mathrm{FBW} = \frac{2\omega_0 L_2^2}{(L_1 + L_2) Z_0}\,. \tag{14}$$

By combining this expression with equations (8) and (13), a nonlinear system of three equations in the unknowns L_1, L_2, and C, that can be efficiently solved through any standard numerical method, is obtained. Finally, given that C must assume a positive value to maintain physical relevance, the following limitations apply:

$$L_2 < L_2^{max} = \frac{\Delta C}{\omega_0^2 C_1 C_2}\,. \tag{15}$$

$$L_1 < L_1^{max} = L_1|_{L_2 = L_2^{max}}\,. \tag{16}$$

$$\mathrm{FBW} < \mathrm{FBW}_{max} = \frac{2\omega_0 (L_2^{max})^2}{Z_0(L_1^{max} + L_2^{max})} \tag{17}$$

C. Derivation of Geometrical Parameters

Under the hypothesis of $\lambda > P \gg w_1, w_2$, and normal incident and linearly polarized wave the lumped elements

[1]If $\Delta C < 0$, the condition (11) is satisfied only when:

$$C_2 > C_1 + \frac{4}{\omega_0^2 L_2}\,. \tag{12}$$

However, under these conditions, equation (10) presents ambiguous solutions. Consequently, a positive capacitance variation ($\Delta C > 0$) is required.

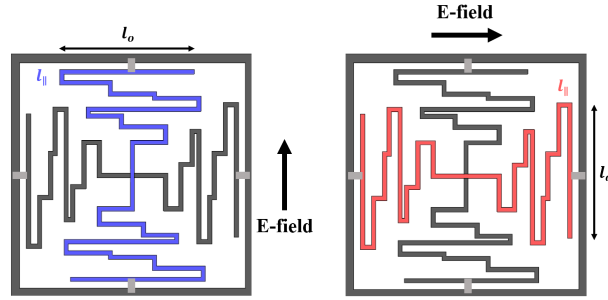

Fig. 5. Illustration of the effective inductive path $l_\parallel$ and capacitive interface length l_o under (a) vertical and (b) horizontal linear polarization. The path $l_\parallel$ identifies the total conductive length supporting current flow aligned with the electric field, while l_o denotes the effective segment orthogonal to the field and coupled to the outer loop.

provided by the ECM can be analytically related to the unit cell geometrical parameters through formulas available in the literatures [33], [34], [35], [36], [37], and [38], depending on the unit cell layout. Specifically, the per-unit length inductance of conductor traces can be expressed as [35]:

$$L_{unit} = \frac{\mu_0 \mu_{eff}}{2\pi} \log\left[\csc\left(\frac{\pi w_1}{2P}\right)\right]\,, \tag{18}$$

where $\mu_0\mu_{eff}$ is the permeability of the medium. For complex geometries, it is essential to identify the portion of the layout that actually supports current flow induced by the incoming electric field to compute the total inductance L_1. For instance, if the incident electric field is vertically polarized, the effective inductive path is given by the vertical branch of the layout that is electrically connected between the top and bottom varactor terminals. This path, denoted as $l_\parallel$, is defined as the total physical length of all conductor segments that form a continuous conductive route between the two opposite sides of the external loop (Fig. 5a). The same considerations apply for horizontally polarized fields, where the relevant current path spans between the lateral varactor terminals (see Fig. 5b). Therefore:

$$L_1 = l_\parallel \cdot L_{unit}\,. \tag{19}$$

In a similar fashion, the inductance associated with the external loop is given by:

$$L_2 = \frac{\mu_0 \mu_{eff} P}{2\pi} \log\left[\csc\left(\frac{\pi w_2}{2P}\right)\right]\,, \tag{20}$$

Finally, the per-unit length capacitance between the inner and outer layouts is:

$$C_{unit} = \frac{C}{l_o} = \frac{2\varepsilon_0 \varepsilon_{eff}}{\pi} \log\left[\csc\left(\frac{\pi s}{2P}\right)\right]\,. \tag{21}$$

where $\varepsilon_0\varepsilon_{eff}$ is the permittivity of the medium, and l_o is the length of the internal layout trace that is orthogonal to the incident electric field E and faces the outer loop (Fig. 5). It corresponds to the conductor segment where the varactor is connected. Finally, the effective permittivity ε_{eff} is calculated through a generalized fitting model as in [39].

D. Use of the Equivalent Circuit Model

The proposed ECM supports both the analysis and synthesis of FSS unit cells by linking design specifications to circuit

Authorized licensed use limited to: Universita degli Studi di Roma Tor Vergata. Downloaded on May 21,2026 at 10:39:51 UTC from IEEE Xplore. Restrictions apply.

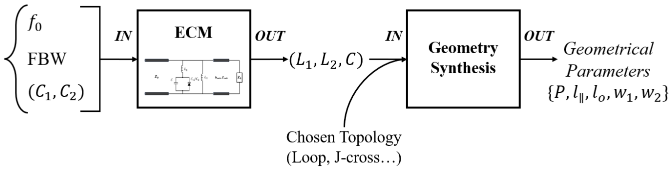

Fig. 6. Block-level design workflow for the proposed ECM.

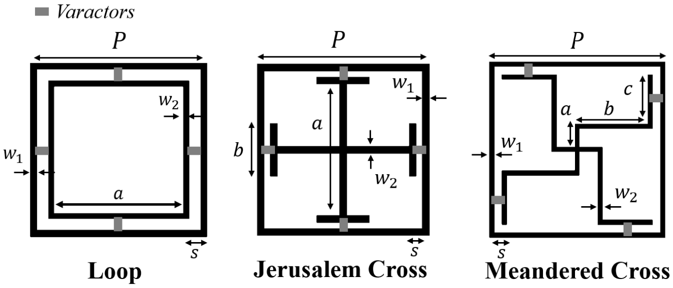

(a) (b) (c)

Fig. 7. Examples of unit cells whose geometry consists of an inductive layout surrounded by an external loop. P is the periodicity of the unit cell, and w_1,w_2 are the trace widths of the outer loop and the inner conductor, respectively.

parameters and physical geometry. The model enables parametric analyses to explore how geometric features affect the lumped elements L_1, L_2, and C, and allows direct computation of these parameters from target values of center frequency f_0, FBW, and varactor capacitances C_1 and C_2. It also assists in evaluating the impact of varactor selection on the achievable tuning range, guiding component choices during the design process.

A possible design workflow (Fig. 6) is reported next:

1) **Circuit Synthesis:** Given f_0, FBW, and the two fixed capacitances C_1, C_2 of the varactor, the model provides the required lumped values (L_1, L_2, C) that enable switching between reflective and transparent states at the same frequency by solving equations (8), (13), and (14). It is worth noticing that the selection of the varactor is of critical importance, since it directly influences achievable periodicity and FBW, imposing critical trade-offs between miniaturization, spectral agility, and the operational frequency limits of the ECM. Thus, an application-driven selection framework is reported in the Appendix.
2) **Geometry synthesis:** The retrieved electrical parameters are translated into the physical layout of the unit cell 3D-model by inverting (19)-(21). Thus, no initial guess for the geometric parameters is required.

This structured approach reduces reliance on time-consuming full-wave iterations and enables fast prototyping of reconfigurable FSSs, even when limited to just two control states.

III. Model Validation

The validity of the proposed ECM-based design tool for binary reconfigurable FSSs is numerically verified through the analysis of three representative examples, each addressing different application constraints. Since the controlling tag (not included in this analysis) can be electrically decoupled from the FSS, the selected unit-cell configurations (Fig. 7) span a broad range of design scenarios in terms of operating frequency, fractional bandwidth (FBW), and physical size. Following the workflow summarized in Fig. 6, the lumped-element values are first derived using (8)–(13) and then mapped into geometric dimensions through (19)–(21), depending on the specific unit-cell layout. Full-wave simulations, performed in CST Microwave Studio 2025 under the assumption of an infinite periodic structure [14], are used to corroborate the model predictions.

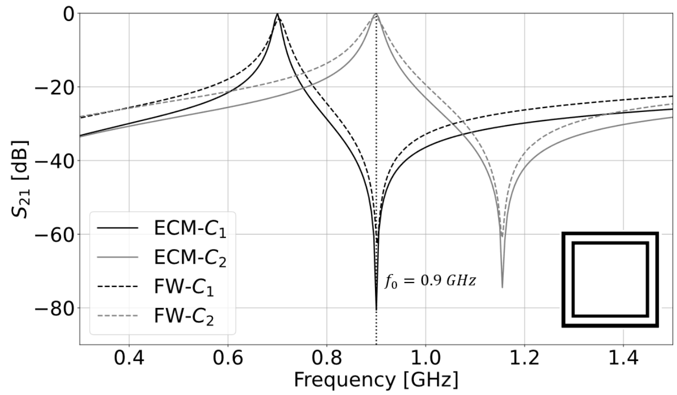

Fig. 8. Comparison between ECM and full-wave (FW) S_{21} for the concentric loops layout.

In all examples, the unit cells are printed on a 1.6 mm-thick FR-4 substrate ($\varepsilon_r = 4.3$, $\tan\delta = 0.025$), with a fixed 0.6 mm spacing between the inner conductor and the outer loop to accommodate the varactor diodes. Varactor models are chosen as detailed in the Appendix (all examples assume varactors whose capacitance can be switched by a control voltage consistent with the output levels of commercial RFID ICs), and all periodicities are expressed in terms of the effective wavelength $\lambda = \lambda_0/\varepsilon_{\text{eff}}$, where λ_0 denotes the free-space wavelength.

A. Double Concentric Loops

The first design example addresses a reconfigurable FSS based on the double concentric loops configuration (Fig. 7a). The design specifications include an operational frequency of $f_0 = 0.9$ GHz and a *narrow-band* transparency (FBW = 2 %). To satisfy these constraints, the SMV1413 varactor diode by Skyworks [40] was selected. This device operates between $C_1 = C(0\,V) = 9.24\,pF$ and $C_2 = C(2\,V) = 5.22\,pF$, offering a favorable trade-off between high capacitance C_1, limited variation $\Delta C \approx 0.4 \cdot C_1$, and compatibility with the targeted frequency (see Appendix). The lumped parameters computed through the proposed ECM are $L_1 = 3\,nH$, $L_2 = 2\,nH$, and $C = 0.95\,pF$. The corresponding geometrical parameters are derived by inverting (19) –(21) with $l_{\parallel} = l_o = a$, resulting in $a = 10\,mm$, $w_1 = 2\,mm$, $w_2 = 0.7\,mm$, and $P = 16.6\,mm \approx 0.1\lambda$.

Fig. 8 and Table I highlight the excellent agreement between the transmission coefficient S_{21} predicted by the ECM and that obtained via full-wave simulation of the 3D unit cell. The shift in the resonant frequency is only 0.2 %, while the FBW extracted from the full-wave model is 3%, differing by merely 1% from the analytical result.

Authorized licensed use limited to: Universita degli Studi di Roma Tor Vergata. Downloaded on May 21,2026 at 10:39:51 UTC from IEEE Xplore. Restrictions apply.

TABLE I
SUMMARY OF ECM VALIDATION RESULTS FOR THE THREE FSS UNIT CELL GEOMETRIES

	Concentric Loops	Jerusalem Cross	Folded Cross
Design Specifications			
f_0 [GHz]	0.90	2.45	0.40
FBW [%]	2	35	7
P/λ	–	–	< 0.1
ECM-Synthesized Parameters			
L_1 [nH]	3.0	3.5	4.9
L_2 [nH]	2.0	6.8	6.0
C [pF]	0.95	0.11	2.9
Full-Wave Results			
Δf_0 [%]	0.2	2.0	5.0
ΔFBW [%]	1	4	1
P/λ	0.10	0.30	0.04

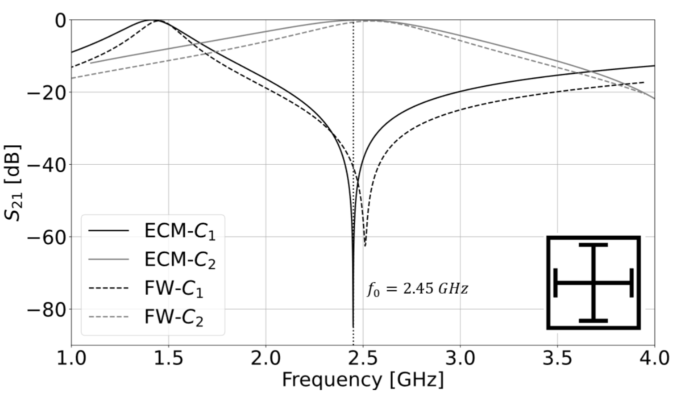

Fig. 9. Comparison between ECM and full-wave (FW) S_{21} for the Jerusalem Cross layout.

B. Jerusalem Cross

As a second design example, a reconfigurable FSS based on the Jerusalem Cross topology is considered (Fig. 7b). The design requirements are the target center frequency $f_0 = 2.45\,\text{GHz}$ and a *wideband* transparency (FBW = 35 %). A suitable varactor diode for this application is the MAVR-000120-1411 by Macom [41], which offers a nominal capacitance range of $C_1 = C(0\,V) = 1.1\,pF$ and $C_2 = C(2\,V) = 0.4\,pF$. This choice is advantageous due to its relatively low nominal capacitance and high tunability, with a capacitance swing of $\Delta C \approx 0.6 \cdot C_1$ (see Appendix). Using the proposed ECM, the synthesized lumped parameters are $L_1 = 3.5\,nH$, $L_2 = 6.8\,nH$, and $C = 0.11\,pF$. To limit the degrees of freedom in the geometry synthesis process, a symmetry constraint $w_1 = w_2 = w$ was enforced, thereby ensuring only three independent geometrical variables. Thus, by imposing $l_{\|} = a$ and $l_o = b$ in (19) –(21), the physical dimensions were hence derived as $a = 10.9\,mm$, $w = 1.7\,mm$, $b = 5\,mm$, and $P = 18.4\,mm \approx 0.3\lambda$.

Again, good agreement is observed between the transmission coefficient S_{21} analytically computed through the circuit model and that obtained from full-wave simulations, as shown in Fig. 9 and in Table I. The resonant frequency derived from the full-wave analysis exhibits a shift of approximately 2 % with respect to the ECM prediction, while the resulting fractional bandwidth is 31 %, slightly lower than that analytically computed.

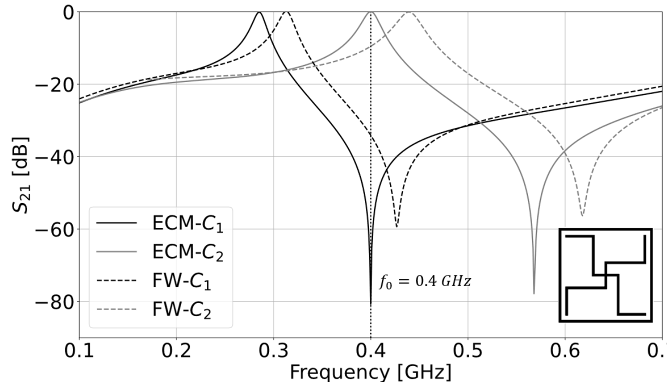

Fig. 10. Comparison between ECM and full-wave (FW) S_{21} for the folded cross layout.

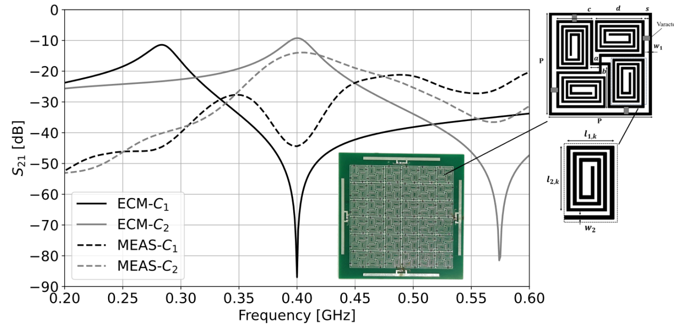

Fig. 11. Comparison between ECM predictions and measured S_{21} for the spiralized folded-cross FSS in [12]. The prototyped layout has the following dimensions: a = 0.9 mm, b = 4.85 mm, c = 4.1 mm, d = 6.4 mm, w = 0.3 mm, $L_{\text{spiral}}^{\text{tot}}$ = 10.7 mm, P = 12.4 mm.

C. Folded Cross

The final example focuses on the design of a unit cell based on a folded-cross geometry, as shown in Fig. 7c. In this case, the target resonance frequency is set to $f_0 = 400$, MHz and a desired fractional bandwidth of FBW = 7 % is specified. In addition, a miniaturization constraint is imposed by requiring the unit-cell periodicity to remain below 0.1λ. This case is intended to demonstrate the synthesis capability of the proposed method under stringent spatial limitations. To meet these goals, the SMV1213 varactor diode by Skyworks [42] was selected, providing a high capacitance $C_1 = 28.9\,pF$ and a moderate capacitance swing $\Delta C = C(0\,V) - C(2\,V) = 18.2\,pF$, according to the recommendations provided in the Appendix. The ECM-based synthesis returned the following equivalent circuit parameters: $L_1 = 4.9\,nH$, $L_2 = 6.0\,nH$, and $C = 2.9\,pF$. The geometry was constrained to three degrees of freedom *(a, c, t)* by imposing $w_1 = w_2 = w$, $b = a + c - w/2$, and $P = 2a + 2c + 3w + 2s$. Then, the layout was derived using (19) –(21) with $l_{\|} = 2(a + b + c)$ and $l_o = c$, resulting in $a = 2.2\,mm$, $b = 6.1\,mm$, $c = 4.2\,mm$, $w = 0.6\,mm$, and $P = 16.6\,mm$, which corresponds to a very compact unit cell with periodicity approximately equal to 0.04λ.

Fig. 10 shows the transmission coefficient obtained from the ECM with full-wave simulations. While the overall agreement remains satisfactory, a more pronounced frequency shift

Authorized licensed use limited to: Universita degli Studi di Roma Tor Vergata. Downloaded on May 21,2026 at 10:39:51 UTC from IEEE Xplore. Restrictions apply.

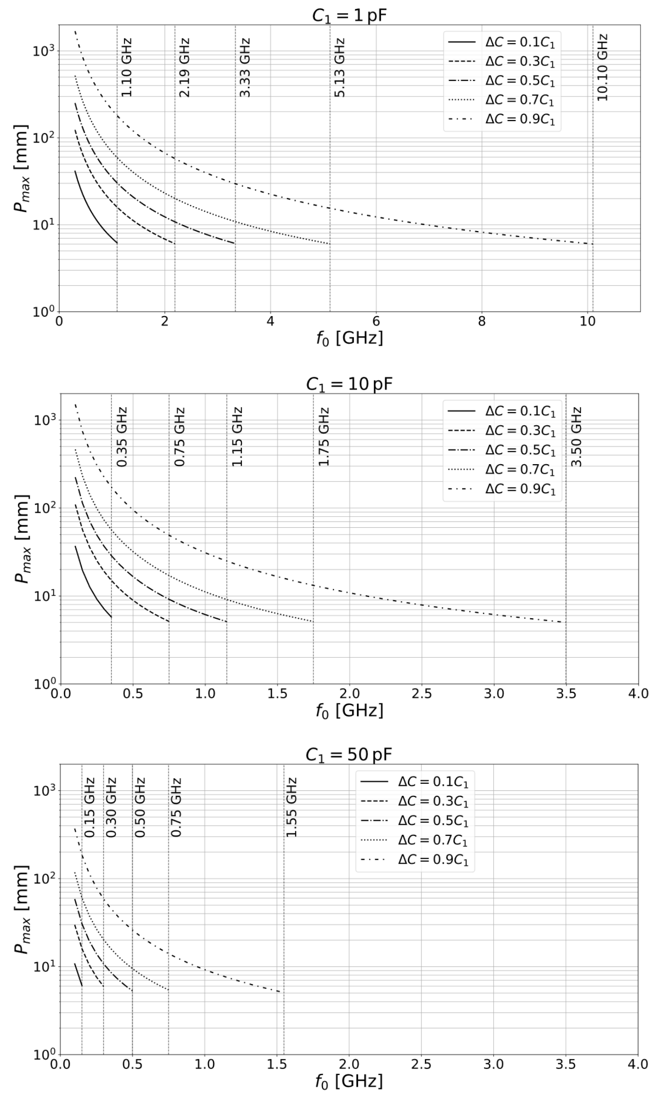

Fig. 12. Maximum admissible periodicity $P_{\max}$ as a function of the operating frequency f_0, evaluated for different combinations of nominal varactor capacitance C_1 and tuning range ΔC. Each subplot corresponds to a fixed C_1 value, while curves represent increasing ΔC. Here $w_1 = 0.5\,mm$.

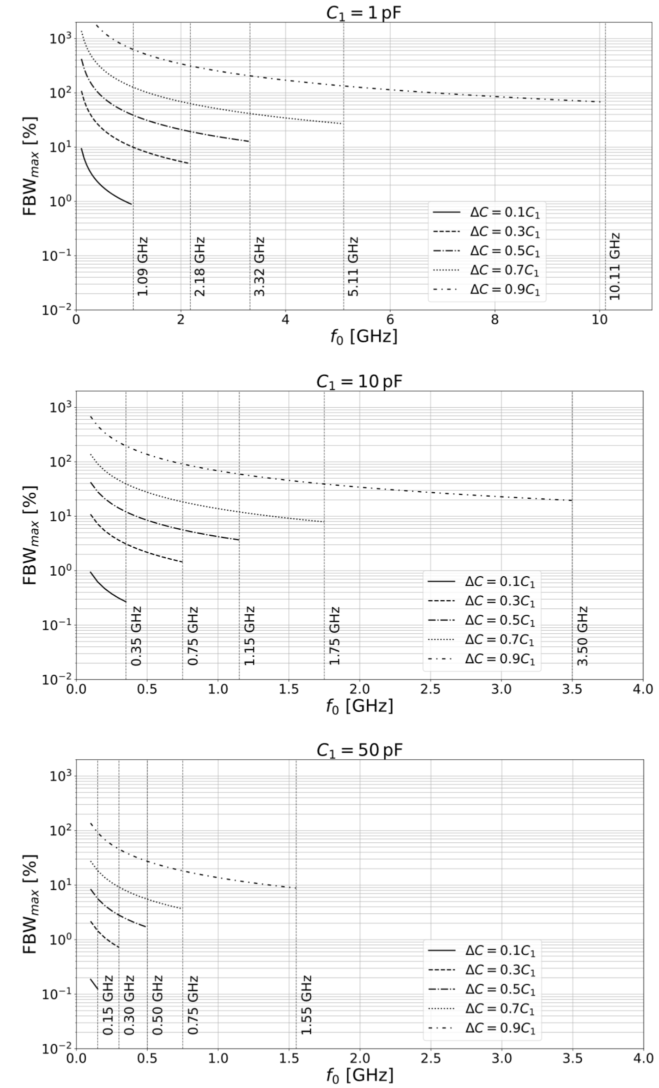

Fig. 13. Maximum fractional bandwidth $\mathrm{FBW}_{\max}$ as a function of the operating frequency f_0, evaluated for different combinations of nominal varactor capacitance C_1 and capacitance swing ΔC. Here $w_1 = 0.5\,mm$.

is observed compared to previous cases, as summarized in Table I. Specifically, the full-wave resonance appears shifted by approximately 5 %, which can be attributed to the complex and folded current paths of the geometry, leading to deviations from the simplified assumptions of the analytical model. However, despite this shift, the resulting structure achieves the desired miniaturization with a simulated FBW of 6 %, close to the arbitrarily chosen target.

D. Miniaturized FSS on a Stratified Medium

To further assess the robustness of the proposed ECM under more realistic electromagnetic conditions, it was applied to a miniaturized folded cross FSS operating on a stratified biological medium, previously reported for epidermal shielding in the MICS band (401–406 MHz) [12]. Unlike the free-space cases, this scenario involves strong miniaturization and multilayer dielectric loading, providing a significantly more demanding benchmark. In this configuration, the FSS is placed over a layered tissue phantom (skin–fat–muscle). Accordingly, the single transmission line section of Fig. 3 is replaced by a cascade of transmission line segments, each characterized by its characteristic impedance $Z_\ell = Z_0/\sqrt{\varepsilon_{r,\ell}}$ and electrical length h_ℓ, where $\varepsilon_{r,\ell}$ and h_ℓ denote the relative permittivity and thickness of the ℓ-th layer [13].

The unit cell considered in [12] derives from the folded-cross layout previously described but incorporates rectangular spiral arms to achieve the required miniaturization (layout in the inset of Fig. 11). The spiral is generated through $K = 2N$ contraction steps, where N is the number of turns. Each step consists of one horizontal and one vertical segment whose lengths decrease monotonically as the spiral approaches the center. If $l_1 = c - 2t$ and $l_2 = d - 2t$ denote the lengths of the outermost turn, the geometry evolves according to $l_{1,k} = l_1 - \Delta(k-1)$ and $l_{2,k} = l_2 - \Delta(k-1)$, with $\Delta = 2t$. The constraints $l_{1,k} < \Delta$ and $l_{2,k} < \Delta$ prevent self-intersections. The total spiral length is $L^{\text{tot}}_{\text{spiral}} = \sum_{k=1}^{2N}(l_{1,k} + l_{2,k})$.

The same target specifications (f_0, FBW), geometric constraints, and varactor pair (C_1, C_2) of Section III-C were used, yielding analogous lumped parameters (L_1, L_2, C). Using the

Authorized licensed use limited to: Universita degli Studi di Roma Tor Vergata. Downloaded on May 21,2026 at 10:39:51 UTC from IEEE Xplore. Restrictions apply.

inversion relations (19) –(21), adapted to the spiralized geometry, the inductive and capacitive paths become $L_{\|} = 2(a + b + c + d + L_{\text{spiral}}^{\text{tot}})$ and $l_o = c$, with the additional geometric constraint $d = P/2 - s + a - 2t$. Solving this system yields the synthesized dimensions $a = 1.3$ mm, $b = 4.6$ mm, $c = 4.1$ mm, $d = 6.4$ mm, $w = 0.95$ mm, $L_{\text{spiral}}^{\text{tot}} = 4.5$ mm, $P = 15$ mm.

Fig. 11 compares the ECM-predicted transmission coefficient with the measured S_{21} of the fabricated prototype reported in [12], after a slight optimization of the geometric parameters required to account for finite-size effects and non-ideal lumped elements. Despite the increased geometric complexity and the strong loading introduced by the multilayer phantom, the ECM preserves good predictive accuracy: the resonance and anti-resonance frequencies, the spectral contrast between the two varactor states, and the transparent-state bandwidth are all reproduced within approximately 4–5%.

IV. Conclusion

This work introduces a compact and generalizable synthesis methodology for designing binary-reconfigurable Frequency Selective Surfaces (FSSs) based on an Equivalent Circuit Model (ECM). The proposed approach enables a semi-analytical synthesis from high-level specifications (target frequency, fractional bandwidth, and varactor capacitances) directly to the physical layout of the unit cell. Beyond drastically reducing the design time, the ECM enables the correct selection of the varactor for miniaturization or bandwidth control under the fixed two-state biasing imposed by RFID chips (see Appendix). This key step, unnecessary in actively biased or FPGA-based systems where the tuning voltage is freely adjustable [26], cannot be obtained from full-wave simulations alone and is essential to guarantee feasibility before any electromagnetic refinement. The methodology has been validated across three representative unit-cell geometries, demonstrating accurate prediction of the FSS response with deviations from full-wave simulations below 5%. In addition, the ECM was extended to handle multilayer dielectric environments and was applied to a miniaturized spiralized FSS placed on a stratified biological phantom. This additional study confirms that the model remains predictive even under strong miniaturization and non-uniform loading conditions, with results consistent with both full-wave simulations and experimentally measured data from the literature.

A key aspect of this study is the assumption that the RFID control tag is electrically decoupled from the FSS. This simplification allows the ECM to remain general-purpose and independent of a specific tag's antenna or placement. While this provides a reliable baseline for the preliminary FSS design, it is acknowledged that further discrepancies may arise from non-ideal component behavior, such as those captured by SPICE models. The practical integration of the RFID front-end, including its positioning and electromagnetic interaction with the surface, is therefore identified as a distinct design challenge. Furthermore, as with traditional periodic structures, the final layout of a finite-sized FSS must also account for truncation effects at its edges and potential coupling between adjacent control tags.

Owing to its low computational burden, analytical transparency, and compatibility with battery-free control, the proposed framework is particularly suitable for emerging applications in embedded, wearable, and secure electromagnetic surfaces. Future work will focus on extending the model to include oblique incidence, polarization reconfigurability, and multilayer implementations, paving the way for the large-scale deployment of battery-free, addressable intelligent surfaces in next-generation RFID infrastructures.

Appendix
Selection of the Varactor Diode

The selection of an appropriate varactor diode is a critical step in the design of reconfigurable FSS unit cells, as it directly affects both the electrical performance and the physical realizability of the structure. This appendix presents a parametric analysis aimed at guiding the designer in choosing the varactor (i.e. the capacitance C_1 and the capacitance swing ΔC) based on application-specific requirements, such as target center frequency, desired miniaturization level, bandwidth and above all RFID ICs driving voltage, tipically comprised between $0 - 2.5V$.

A. Maximum Periodicity P_{max}

The maximum allowable periodicity P_{max}, i.e., the geometrical upper bound of the unit cell directly related to the overall FSS footprint, is a function of f_0, varactor capacitance C_1, capacitance variation ΔC, and the outer loop trace width w_1:

$$P_{max} = f(f_0, C_1, \Delta C, w_1). \tag{22}$$

Fig.12 illustrates the variation of the maximum allowed periodicity $P_{\max}$ as a function of f_0 for a discrete set of representative values of $C_1 = \{1, 10, 50\}$ pF and various ΔC. For consistency, the trace width is fixed at $w_1 = 0.5$ mm, and the periodicity values are constrained by the condition $P_{\max} \geq 10\ w_1$.

An increase in C_1 leads to a systematic reduction in the allowed periodicity. This trend arises from the inverse dependence of the resonant frequency on the equivalent inductance: larger capacitance values reduce the inductance necessary to maintain resonance at a fixed f_0. Since inductance is primarily governed by the length and geometry of the conductive paths, a lower L_{eq} permits a more compact unit cell. Consequently, higher C_1 values support stronger miniaturization, which is advantageous when physical footprint is a limiting constraint. However, as C_1 increases and $P_{\max}$ decreases, the validity of the circuit model is progressively undermined at higher frequencies, where the assumption $P_{\max} \gg w_1$ no longer holds. This establishes a fundamental trade-off: increasing C_1 enables more compact designs, but restricts the upper frequency limit for which the ECM remains accurate and predictive.

The capacitance swing $\Delta C = C_1 - C_2$, which defines the varactor's tuning range, plays a key role in shaping the unit-cell geometry required to support both resonant states at a fixed operating frequency f_0. Numerical results indicate that increasing ΔC leads to a monotonic increase in the maximum periodicity $P_{\max}$. This is because a larger ΔC widens the

Authorized licensed use limited to: Universita degli Studi di Roma Tor Vergata. Downloaded on May 21,2026 at 10:39:51 UTC from IEEE Xplore. Restrictions apply.

separation between the two resonance frequencies, enhancing the electromagnetic contrast but also demanding a broader inductance span to preserve resonance in both states. As inductance in planar layouts is governed by trace length and current path complexity, this requirement inherently calls for a larger unit cell.

B. Maximum Fractional Bandwidth FBW_{max}

The achievable FBW of the synthesized unit cell is bounded between two limits. The upper bound, defined in (17), depends on the resonance condition for the two capacitance states:

$$\mathrm{FBW}_{\max} = f(f_0, C_1, \Delta C). \tag{23}$$

The lower bound is determined by enforcing the minimum admissible periodicity in (20) and evaluating (17) accordingly:

$$\mathrm{FBW}_{\min} = f(f_0, C_1, \Delta C, w_1). \tag{24}$$

Fig.13 presents the parametric trends of $\mathrm{FBW}_{\max}$ for $C_1 = \{1, 10, 50\}$ pF, with fixed trace width $w_1 = 0.5$ mm. The lower bound $\mathrm{FBW}_{\min}$ is shown as a constraint.

For a fixed capacitance swing ΔC, increasing C_1 compresses the FBW. This occurs because the relative difference between C_1 and C_2 decreases, reducing the separation between the corresponding resonant frequencies. At high C_1, even large ΔC values yield limited spectral contrast, further narrowing the bandwidth. In contrast, increasing ΔC has a strong, monotonic effect on FBW. Larger swings produce greater shifts in the resonance condition, widening the spectral gap between states and enhancing reconfigurability. This effect is especially pronounced at low C_1, where ΔC constitutes a larger relative change.

In summary, while higher C_1 supports geometric miniaturization, it limits spectral agility; conversely, increasing ΔC improves bandwidth but requires larger unit-cell periodicities. Additionally, the maximum frequency for which the ECM remains valid is jointly constrained by C_1, ΔC, and f_0. As such, varactor selection must balance layout constraints, target frequency, and the desired FBW within the model's validity range.

References

[1] F. Lestini, G. Marrocco, and C. Occhiuzzi, "RFID-based reconfigurable electromagnetic devices," *IEEE J. Radio Freq. Identificat.*, vol. 8, pp. 226–234, 2024.

[2] *Em4152 Datasheet*. Accessed: Jan. 2025. [Online]. Available: https://www.emmicroelectronic.com/sites/default/files/products/datasheets/4152-DS%20v4.2.pdf

[3] *Em4325 Datasheet*. Accessed: Jan. 2025. [Online]. Available: https://www.emmicroelectronic.com/sites/default/files/products/datasheets/4325-DS%20%28updated%20datasheet%20Feb%202023%29.pdf

[4] F. Lestini, A. DiCarlofelice, P. Tognolatti, G. Marrocco, and C. Occhiuzzi, "An RFID-based guided control node for batteryless reconfigurable RF architectures," *IEEE Trans. Microw. Theory Techn.*, early access, Nov. 10, 2025, doi: 10.1109/TMTT.2025.3627440.

[5] A. Sample and J. R. Smith, "Experimental results with two wireless power transfer systems," in *Proc. IEEE Radio Wireless Symp.*, Jan. 2009, pp. 16–18.

[6] Z. X. Wang et al., "A long-range and nearly passive RFID-controlled information metasurface," *Adv. Opt. Mater.*, vol. 12, no. 6, Feb. 2024, Art. no. 2203114.

[7] F. Lestini, G. Marrocco, and C. Occhiuzzi, "Varactor-tunable RFID-based wireless programmable frequency selective surface as a smart shield for implanted medical devices," in *Proc. 19th Eur. Conf. Antennas Propag. (EuCAP)*, Mar. 2025, pp. 1–4.

[8] S. Alamdar et al., "A 16 × 16 array composed of 4 × 4 fully scalable reconfigurable intelligent surfaces (RIS) for 2.4 GHz Wi-Fi using RFID distributed control," *IEEE Trans. Microw. Theory Techn.*, vol. 73, no. 8, pp. 5507–5520, Aug. 2025.

[9] C. Shen, Z. Wang, J. Wu, Q. Cheng, and T. Tao Ye, "Exploring RFID technology for wireless control of smart antennas," *IEEE Internet Things J.*, vol. 11, no. 18, pp. 29757–29765, Sep. 2024.

[10] J. Tong, X. Zhao, Z. Wang, D. Dai, Z. An, and L. Yang, "Commercial RFIDs as reconfigurable intelligent surfaces," in *Proc. IEEE INFOCOM Conf. Comput. Commun.*, May 2025, pp. 1–10.

[11] C. Shen, Z. Wang, L. Yang, F. Mei, and T. T. Ye, "Wirelessly pattern reconfigurable Yagi antenna based on radio frequency identification," *Int. J. Antennas Propag.*, vol. 2024, pp. 1–7, Mar. 2024.

[12] F. Lestini, G. Marrocco, and C. Occhiuzzi, "Passive wireless programmable FSS for adaptive electromagnetic shielding of implanted medical devices," *IEEE J. Electromagn., RF Microw. Med. Biol.*, early access, Sep. 17, 2025, doi: 10.1109/JERM.2025.3604080.

[13] F. Lestini, G. Marrocco, and C. Occhiuzzi, "An equivalent circuit model for designing wireless programmable FSS for WPT EMI suppression and secure communication of implanted devices," in *Proc. IEEE Wireless Power Technol. Conf. Expo (WPTCE)*, Jun. 2025, pp. 1–4.

[14] B. A. Munk, *Frequency Selective Surfaces: Theory and Design*. Hoboken, NJ, USA: Wiley, 2005.

[15] W.-J. Liao, W.-Y. Zhang, Y.-C. Hou, S.-T. Chen, C. Y. Kuo, and M. Chou, "An FSS-integrated low-RCS radome design," *IEEE Antennas Wireless Propag. Lett.*, vol. 18, pp. 2076–2080, 2019.

[16] M. Pazokian, N. Komjani, and M. Karimipour, "Broadband RCS reduction of microstrip antenna using coding frequency selective surface," *IEEE Antennas Wireless Propag. Lett.*, vol. 17, pp. 1382–1385, 2018.

[17] S. M. A. Momeni Hasan Abadi, K. Ghaemi, and N. Behdad, "Ultra-wideband, true-time-delay reflectarray antennas using ground-plane-backed, miniaturized-element frequency selective surfaces," *IEEE Trans. Antennas Propag.*, vol. 63, no. 2, pp. 534–542, Feb. 2015.

[18] P. Megh Sainadh, A. Sharma, and S. Ghosh, "Polarization-insensitive absorptive/transmissive reconfigurable frequency selective surface with embedded biasing," *IEEE Antennas Wireless Propag. Lett.*, vol. 22, pp. 164–168, 2023.

[19] Y. Li, P. Ren, R. Chen, B. Xu, Z. Xiang, and M. Wang, "Design of miniaturized frequency selective rasorber based on complementary bandpass FSS for 5G applications," *IEEE Trans. Electromagn. Compat.*, vol. 66, no. 2, pp. 636–639, Apr. 2024.

[20] J. Yang and Z. Shen, "A thin and broadband absorber using double-square loops," *IEEE Antennas Wireless Propag. Lett.*, vol. 6, pp. 388–391, 2007.

[21] M. Euler and V. F. Fusco, "Frequency selective surface using nested split ring slot elements as a lens with mechanically reconfigurable beam steering capability," *IEEE Trans. Antennas Propag.*, vol. 58, no. 10, pp. 3417–3421, Oct. 2010.

[22] M. Li, Z. Zhang, M.-C. Tang, L. Zhu, and N.-W. Liu, "Bandwidth enhancement and size reduction of a low-profile polarization-reconfigurable antenna by utilizing multiple resonances," *IEEE Trans. Antennas Propag.*, vol. 70, no. 2, pp. 1517–1522, Feb. 2022.

[23] C. Güler, S. Esen Bayer Keskin, and N. Türker Tokan, "Dynamic frequency switching of a bandstop reconfigurable frequency selective surface with PIN diodes for C/X and Ku-band shielding applications," *AEU - Int. J. Electron. Commun.*, vol. 183, Aug. 2024, Art. no. 155402.

[24] X. Chen, J. Tan, L. Kang, F. Tang, M. Zhao, and N. Kato, "Frequency selective surface toward 6G communication systems: A contemporary survey," *IEEE Commun. Surveys Tuts.*, vol. 26, no. 3, pp. 1635–1675, 3rd Quart., 2024.

[25] M. A. Shukoor and S. Dey, "Wideband reconfigurable multifunctional absorber/reflector with bandpass/bandstop filtering and band-notch absorption for RCS and EMI shielding," *IEEE Trans. Electromagn. Compat.*, vol. 66, no. 1, pp. 153–160, Feb. 2024.

[26] A. Ebrahimi, Z. Shen, W. Withayachumnankul, S. F. Al-Sarawi, and D. Abbott, "Varactor-tunable second-order bandpass frequency-selective surface with embedded bias network," *IEEE Trans. Antennas Propag.*, vol. 64, no. 5, pp. 1672–1680, May 2016.

[27] A. Kapoor, R. Mishra, and P. Kumar, "Frequency selective surfaces as spatial filters: Fundamentals, analysis and applications," *Alexandria Eng. J.*, vol. 61, no. 6, pp. 4263–4293, Jun. 2022.

Authorized licensed use limited to: Universita degli Studi di Roma Tor Vergata. Downloaded on May 21,2026 at 10:39:51 UTC from IEEE Xplore. Restrictions apply.

[28] S. C. Bakshi, D. Mitra, and F. L. Teixeira, "FSS-based fully reconfigurable rasorber with enhanced absorption bandwidth and simplified bias network," *IEEE Trans. Antennas Propag.*, vol. 68, no. 11, pp. 7370–7381, Nov. 2020.

[29] D. Ferreira, R. F. D. S. Caldeirinha, I. Cuiñas, and T. R. Fernandes, "Tunable square slot FSS EC modelling and optimisation," *IET Microw., Antennas Propag.*, vol. 11, no. 5, pp. 737–742, Apr. 2017.

[30] F. Bayatpur and K. Sarabandi, "A tunable metamaterial frequency-selective surface with variable modes of operation," *IEEE Trans. Microw. Theory Techn.*, vol. 57, no. 6, pp. 1433–1438, Jun. 2009.

[31] J. Bonache, I. Gil, J. García-García, and F. Martín, "Compact microstrip band-pass filters based on semi-lumped resonators," *IET Microw., Antennas Propag.*, vol. 1, no. 4, pp. 932–936, Aug. 2007.

[32] J.-S. G. Hong and M. J. Lancaster, *Microstrip Filters for RF/Microwave Applications*. Hoboken, NJ, USA: Wiley, 2004.

[33] F. Costa, A. Monorchio, and G. Manara, "An overview of equivalent circuit modeling techniques of frequency selective surfaces and metasurfaces," *Appl. Comput. Electromagn. Soc. J.*, vol. 29, no. 12, pp. 960–976, Dec. 2014.

[34] D. Ferreira, R. F. S. Caldeirinha, I. Cuiñas, and T. R. Fernandes, "Square loop and slot frequency selective surfaces study for equivalent circuit model optimization," *IEEE Trans. Antennas Propag.*, vol. 63, no. 9, pp. 3947–3955, Sep. 2015.

[35] Y. Xu and M. He, "Design of multilayer frequency-selective surfaces by equivalent circuit method and basic building blocks," *Int. J. Antennas Propag.*, vol. 2019, pp. 1–13, Aug. 2019.

[36] I. Anderson, "On the theory of self-resonant grids," *Bell Syst. Tech. J.*, vol. 54, no. 10, pp. 1725–1731, Dec. 1975.

[37] D. F. Sievenpiper, *High-Impedance Electromagnetic Surfaces*. Los Angeles, CA, USA: University of California, 1999.

[38] M. Hosseini and M. Hakkak, "Characteristics estimation for Jerusalem cross-based artificial magnetic conductors," *IEEE Antennas Wireless Propag. Lett.*, vol. 7, pp. 58–61, 2008.

[39] F. Costa, "A simple effective permittivity model for metasurfaces within multilayer stratified media," *IEEE Trans. Antennas Propag.*, vol. 69, no. 8, pp. 5148–5153, Aug. 2021.

[40] *SMV1405 To SMV1430 Series: Plastic-Packaged Abrupt Junction Tuning Varactors*. Accessed: May 2025. [Online]. Available: https://d1ehax0mqsd4rz.cloudfront.net/-/media/SkyWorks/Documents/Products/101-200/SMV1405_1430_Series_200068W.pdf?rev=31bb9fb247f74276bfa2b10ef9ca1360

[41] *MAVR-000120-1411*. Accessed: May 2025. [Online]. Available: https://cdn.macom.com/datasheets/MAVR-000120-1411.pdf

[42] *SMV121x Series: Hyperabrupt Junction Tuning Varactors*. Accessed: May 2025. [Online]. Available: https://d1ehax0mqsd4rz.cloudfront.net/-/media/SkyWorks/Documents/Products/101-200/SMV121x-Series_200057W.pdf?rev=7ba61abd5a9948f283b33acbd89b7918

Francesco Lestini (Member, IEEE) received the B.S. and M.S. degrees (Hons.) in medical engineering from the University of Rome Tor Vergata, Rome, Italy, in 2019 and 2021, respectively, where he is currently pursuing the Ph.D. degree in computer science, control, and geoinformation with the Pervasive Electromagnetics Laboratory. Since 2023, he has been a part-time Research and Development RF Engineer with RADIO6ENSE Srl. His research interests include the wireless reconfiguration of electromagnetic devices using RFID technology and developing epidermal RFID grids for measuring skin temperature distribution. He is also part of the Cyber4Health Observatory, which focuses on raising international awareness about the need for pre-market regulations related to the cyber and physical security of medical devices. He won the Best Paper Award at the Seventh Edition of SpliTech Conference in 2022 on smart and sustainable technologies, the Gaetano Latmiral Award at the XXV Riunione Nazionale di Elettromagnetismo (RiNEm) in 2024, the Huawei Tech Arena Italy in 2024, and the Best Student Paper Award at IEEE RFID-TA in 2025.

Gaetano Marrocco (Senior Member, IEEE) received the M.Sc. degree in electronic engineering and the Ph.D. degree in applied electromagnetics from the University of L'Aquila, Italy, in 1994 and 1998, respectively.

He was a Researcher at the University of Rome Tor Vergata from 1994 to 2014, an Associate Professor of electromagnetics from 2013 to 2017, a Guest Professor at the University of Paris-Est Marne-la-Vallée in 2015, and has been a Full Professor at the University of Rome Tor Vergata since 2018. From 2018 to 2024, he was the Director of the Medical Engineering School. He is currently the Deputy Director of the Department of Civil Engineering and Computer Science. He is also the Director of the Pervasive Electromagnetics Laboratory (pervasive.ing.uniroma2.it) and the Co-Founder and the President of the university spin-off RADIO6ENSE (www.radio6ense.com), which is active in the short-range electromagnetic sensing for the Industrial Internet of Things, smart manufacturing, automotive bioengineering, and pharma. The first phase of his research career was devoted to the modelling and designing of structural broadband and ultra-wideband antennas for satellite (ESA, ASI), avionic, and naval (Leonardo) communications. Since 2003, he has been investigating sensor-oriented miniaturized antennas for biomedical engineering and radiofrequency identification (RFID), contributing to the move from the RF labelling of objects to the passive sensor networks in the Internet of Things era. He carried out pioneering research on bodycentric battery-less wireless sensors concerning textile RFID antennas, tattoo-like sensors (flexible and stretchable epidermal electronics), and radio-sensors embedded inside implantable prostheses. He was a member of the IEEE Antennas and Propagation Society Awards Committee. Moreover, he is the Chair of Italian delegation URSI Commission D Electronics and Photonics. He was the Chair of the Local Committee of the V European Conference on Antennas and Propagation (EUCAP-2011); the TPC Chair of the 2012 IEEE-RFID TA in Nice, France; the TPC Track-Chair of the 2016 IEEE Antennas and Propagation International Symposium and the IEEE-RFID 2018 USA; and the General Co-Chair of the IEEE Flexible, Printable Sensors and Systems (FLEPS) in Tampere, Finland, in 2024. He is listed in the PLOS ranking of Top 1.5% Scientists Worldwide (source University Stanford, 2024) and in the first three places on ScholarGPs for worldwide RFID impact in 2024. He served as an Associate Editor for IEEE ANTENNAS AND WIRELESS PROPAGATION LETTERS and IEEE JOURNAL OF RADIOFREQUENCY IDENTIFICATION. Currently, he is an Associate Editor for IEEE JOURNAL OF FLEXIBLE ELECTRONICS.

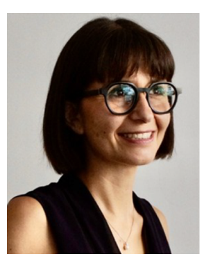

Cecilia Occhiuzzi (Member, IEEE) received the M.Sc. and Ph.D. degrees in medical engineering from the University of Rome Tor Vergata, Rome, Italy, in 2008 and 2011, respectively. She is currently an Associate Professor with the University of Rome Tor Vergata, where she teaches electromagnetic fields, biomedical interaction, and instrumentation and techniques for health monitoring and therapy. She is also the Co-Founder and the CEO of RADIO6ENSE, a spin-off of the University of Tor Vergata active in RFID solutions for the industrial sector. She has co-authored more than 80 papers in international journals and conferences and ten patents on RFID sensing systems. Her research interests include wireless health monitoring through wearable and implantable radio frequency/mm-wave identification techniques and pervasive sensing paradigms for the food sector and industry 4.0. She is listed in the PLOS 2023 ranking of the Top 2% Scientists Worldwide.

Authorized licensed use limited to: Universita degli Studi di Roma Tor Vergata. Downloaded on May 21,2026 at 10:39:51 UTC from IEEE Xplore. Restrictions apply.